

Article

Combining Remote Sensing Data and Geochemical Properties of Ultramafics to Explore Chromite Ore Deposits in East Oltu Erzurum, Turkey

Amr Abd El-Raouf ^{1,*}, Fikret Doğru ², Özgür Bilici ³, Islam Azab ⁴, Sait Taşci ², Lincheng Jiang ⁵, Kamal Abdelrahman ⁶, Mohammed S. Fnais ⁶ and Omar Amer ¹

- ¹ Geology Department, Faculty of Science, Zagazig University, Zagazig 44519, Egypt; omaramer@science.zu.edu.eg
- ² Oltu Vocational College, Ataturk University, Construction, 25400 Erzurum, Turkey; fikretdogru@atauni.edu.tr (F.D.); saittasci@atauni.edu.tr (S.T.)
- ³ Department of Engineering, Civil Engineering, Ataturk University, 25050 Erzurum, Turkey; ozgurbilici@atauni.edu.tr
- ⁴ Nuclear Materials, Authority, El-Maadi, Kattamiya, Cairo 11884, Egypt; islam_nma2010@yahoo.com
- ⁵ School of Emergency Management, Xihua University, Chengdu 610039, China; jianglc@mail.xhu.edu.cn
- ⁶ Department of Geology and Geophysics, College of Science, King Saud University, P.O. Box 2455, Riyadh 11451, Saudi Arabia; khassanein@ksu.edu.sa (K.A.); mfnais@ksu.edu.sa (M.S.F.)
- * Correspondence: ammohammed@science.zu.edu.eg

Abstract: The present research's main objective was to apply thorough exploration approaches that combine remote sensing data with geochemical sampling and analysis to predict and identify potential chromitite locations in a complex geological site, particularly in rugged mountainous terrain, and differentiate the ultramafic massif containing chromitite orebodies from other lithologies. The ultramafic massif forming the mantle section of the Kırdağ ophiolite, located within the Erzurum–Kars Ophiolite Zone and emerging in the east of Oltu district (Erzurum, NE Turkey), was selected as the study area. Optimum index factor (OIF), false-color composite (FCC), decorrelation stretch (DS), band rationing (BR), minimum noise fraction (MNF), and principal and independent component analyses (PCA-ICA) were performed to differentiate the lithological features and identify the chromitite host formations. The petrography, mineral chemistry, and whole-rock geochemical properties of the harzburgites, which are the host rocks of chromitites in the research area, were evaluated to verify and confirm the remote sensing results. In addition, detailed petrographic properties of the pyroxenite and chromitite samples are presented. The results support the existence of potential chromitite formations in the mantle section of the Kırdağ ophiolite. Our remote sensing results also demonstrate the successful detection of the spectral anomalies of this ultramafic massif. The mineral and whole-rock geochemical features provide clear evidence of petrological processes, such as partial melting and melt–peridotite interactions during the harzburgite formation. The chromian spinels' Cr#, Mg#, Fe³⁺, Al₂O₃, and TiO₂ concentrations indicate that the harzburgite formed in a fore-arc environment. The Al₂O₃ content and Mg# of the pyroxenes and the whole-rock Al₂O₃/MgO ratio and V contents of the harzburgite are also compatible with these processes. Consequently, the combined approaches demonstrated clear advantages over conventional chromitite exploration techniques, decreasing the overall costs and supporting the occurrence of chromite production at the site.

Keywords: remote sensing; ophiolite; geochemistry; ultramafics; chromitite; Turkey



Citation: El-Raouf, A.A.; Doğru, F.; Bilici, Ö.; Azab, I.; Taşci, S.; Jiang, L.; Abdelrahman, K.; Fnais, M.S.; Amer, O. Combining Remote Sensing Data and Geochemical Properties of Ultramafics to Explore Chromite Ore Deposits in East Oltu Erzurum, Turkey. *Minerals* **2024**, *14*, 1116. <https://doi.org/10.3390/min14111116>

Academic Editor: Paul Alexandre

Received: 5 August 2024

Revised: 25 October 2024

Accepted: 29 October 2024

Published: 2 November 2024



Copyright: © 2024 by the authors. Licensee MDPI, Basel, Switzerland. This article is an open access article distributed under the terms and conditions of the Creative Commons Attribution (CC BY) license (<https://creativecommons.org/licenses/by/4.0/>).

1. Introduction

There are vast amounts of ophiolitic rocks in Turkey. Based on the findings of [1], chromite (Cr) is only found in mafic and ultramafic igneous rocks. Variable degrees of serpentinization are frequently seen in these ultramafic rocks [2–5].

Ophiolites are components of the oceanic crust and the outer mantle that were moved and formed continents during geological processes known as orogenic events [6,7]. Ophiolitic sequences are typically found in suture areas and can reassemble the ancient location of orogenic activities [7,8] (Figure 1a). Typically, they contain a variety of mineral deposits, including chromite deposits. These types of deposits comprise tiny masses of molten rock that are not evenly spread out throughout the ultramafic region of an ophiolite system [5,6]. Most of these deposits are located close to the mantle transition region, specifically within the ultramafic rocks (mostly dunite) of the ophiolitic pattern and at the boundary of higher regions that resemble cumulates [9,10].

The mining of surficial deposits has a long history, and geophysical approaches have faced several difficulties, including the small size of chromite pods, their resemblance to certain rocks, structural features, and the potential presence of iron-rich bodies. Despite these difficulties, various approaches to mineral exploration have been developed, with significant accuracy and success [10,11]. Due to their ability to extend above the rocks surrounding them and their greater resistance to weathering than their serpentinized host, most surficial chromite deposits have been exploited. However, the fact that such deposits are usually discovered in clusters raises the likelihood that there are other orebodies far below the deposits that have been identified. In addition, no single investigation technique can be used to identify such deposits because of the complexity of the relevant geologic processes. Conversely, combined methods have been relatively successful for chromite exploration; one such example is the fusion of geological, geochemical, remote sensing, and geophysical approaches [11–13].

The ideal method for detecting these serpentinized sites in dry locations without vegetative cover and mapping regions with irregular topography is remote sensing [14–16]. Satellite remote sensing has demonstrated its ability to differentiate between hydrothermal alteration areas, structures, and lithologies to significantly differentiate serpentinized peridotites from other ultramafic and mafic rocks, intending to determine exploration possibilities [17,18]. Podiform chromite exploration has benefited from some established techniques, in addition to the advancement of satellite missions and their multiple uses in the remote sensing of indications of mineralization [19]. Furthermore, some of the essential characteristics of podiform chromite, such as the lack of significant hydrothermal alteration associated with mineralization, continue to be a challenge. Principal Component Analysis (PCA), band rationing, and spectral transform methods have been the mainstays of traditional lithological mapping techniques employed in most ophiolite remote sensing investigations [15,16,20].

To more definitively define the criteria for identifying mineralized zones containing chromite, through the current study, we aim to establish a link between satellite remote sensing, geochemical analysis, and field data. This strategy becomes crucial in locations with rugged terrains, such as those examined in this case study (Oltu Erzurum's East, Turkey). We used a multi-stage processing approach to accomplish this goal. First, we used satellite remote sensing to identify the most promising lithological units (serpentinized ultramafic units) that could host chromite mineralization. Furthermore, we conducted field surveys, petrographic analyses, and geochemical evaluations to assess the reliability of the data. After integrating the data, we were able to generate a geological map that included more chromite prospecting sites for ultramafics.

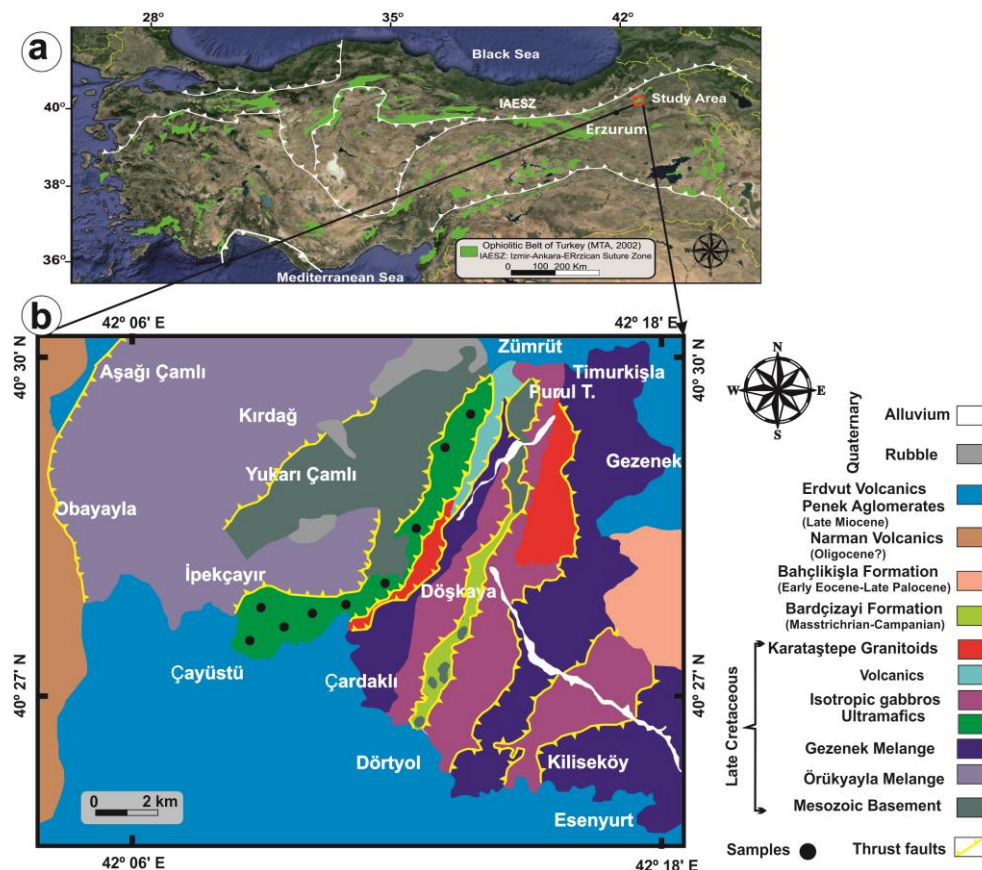


Figure 1. (a) Illustration depicting the overall distribution of ophiolite belts and prominent tectonic suture areas across Turkey, with modifications derived from [21,22]. (b) Geological map specifically detailing the Kırdağ ophiolite, adapted from [23].

2. Geological Outlines

The Eastern Pontides and Eastern Taurides are critical tectonic zones in the northeastern Anatolian Area [24]. The Eastern Pontide Belt has been recognized as part of the Sakarya Region, forming a segment of the active continental margin of Eurasia [25]. This margin evolved due to the northward subduction of Neotethys during the Late Cretaceous [24–27]. Although scholarly opinions vary regarding its geodynamic evolution, some suggest southward subduction from the Palaeozoic to the end of the Eocene period [28]. The Late Cretaceous ophiolites with ophiolitic melange found in the Izmir–Ankara–Erzincan Suture Zone (IAESZ) divide the Pontide and Tauride tectonic zones [24,25,29–33] (Figure 1a). The Eastern Pontides' eastern section is made up of four lithological sub-groups: the Late Cretaceous ophiolites, the upper mixed portion, the lower mixed portion, and the autochthonous units of the Eastern Pontides [27]. The Late Cretaceous ophiolites—the Erzurum–Kars Ophiolite Zone—consist of ophiolitic melange and metamorphic and sedimentary formations [23].

The Kırdağ ophiolite sequence, including the study area and situated in the Erzurum–Kars Ophiolite Zone, commences with gabbroic rocks at the bottom, overlain by basal conglomerates that are approximately 50 cm thick. Subsequently, the Bardızçayı Formation comprises sandstone, mudstone, shale, siltstone, and radiolarite [23]. The upper part of the sequence contains blocks of limestone and ophiolitic segments. The Gezenek melange unit comprises various volcanic components: granitoid, gabbro, diabase, serpentinite, chert, sandstone, tuff, and siltstone [23]. The ultramafic rocks predominantly consist of serpentinized harzburgites with minor occurrences of wherlite, dunite, chromitite, and pyroxenite [23,34]. These ultramafics and related rocks are structurally positioned on the Gezenek melange, a tectonic unit hosting diverse lithologies. In addition to pyroxenites, which intrude into peridotites, diabase and gabbroic veins are present in the area [23,35].

The Late Cretaceous Karataştepe Granitoid also led to the development of low-grade metamorphic rocks comprising basic volcanics and volcanoclastic and sedimentary formations in the region [23,31,32,35] (Figure 1b).

3. Materials and Methods

3.1. Remote Sensing Data

Field and laboratory investigations were combined using ASTER level 1B data. ASTER measures electromagnetic radiation in 14 spectral bands to create images of the Earth's surface and atmosphere. Three visible and near-infrared (VNIR) bands range from 0.52 to 0.86 μm , with a 15 m spatial resolution. In addition, six SWIR bands (1.6–2.43 μm) are available, with a spatial resolution of 30 m. Five TIR bands span 8.125–11.65 μm wavelengths, with a 90 m spatial resolution. By adding a band that captures visible and near-infrared light, digital elevation models (DEMs) can be created by utilizing the bands 3N and 3B. Each ASTER scene covers an area of 60 \times 60 km due to its 60 km sweep width. As indicated, these characteristics render it appropriate for the application of regional mapping, as stated by the authors of [36–38]. Cloud-free scenes of corrected ASTER level 1 precision terrain registered at sensor radiance (AST_L1T) and covering the study area were downloaded for free on 4 June 2024 from the USGS Earth Explorer website (<https://earthexplorer.usgs.gov>), accessed on 23 June 2024.

3.1.1. ASTER Data Preprocessing

The ASTER raw dataset, consisting of visible and near-infrared (VNIR) and shortwave infrared (SWIR) data, underwent preprocessing procedures to prepare it for further processing and analysis. The preprocessing stage comprises radiometric calibration, atmospheric correction, and minimal noise fraction (MNF). ENVI software version 5.3 by L3Harris Geospatial USA (Broomfield, CO, USA) was used to apply radiometric calibration and the fast line-of-sight atmospheric analysis of spectral hypercubes (FLAASH) atmospheric correction model. This process, described in [39], involved calibrating ASTER data to spectral appearance, subsetting, and converting the digital number (DN) to reflectance. ASTER's (TIR) bands underwent radiometric calibration and thermal atmospheric correction (Figure 2).

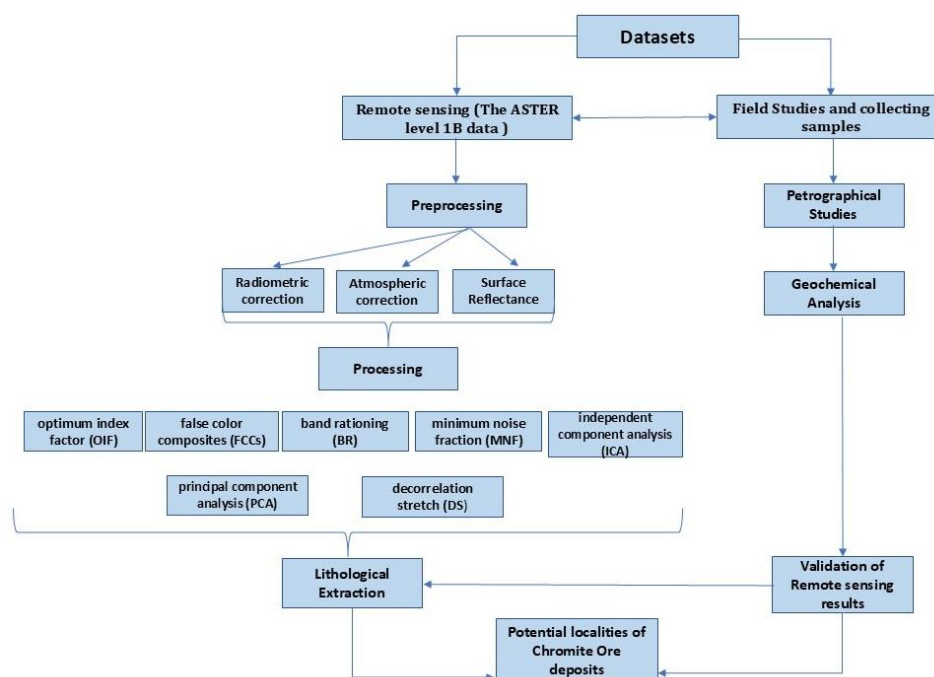


Figure 2. A flow chart showing the methodology of the combined approach applied in the investigated area.

3.1.2. Image Processing

In this study, we employed various techniques that exploit different mechanisms to enhance image quality. These approaches cover (OIF), (FCC), (BR), (MNF), (ICA), (PCA), and (DS) (Figure 2).

3.1.3. Optimum Index Factor (OIF)

Depending on their overall variance and their correlation coefficient, the OIF method evaluates and ranks every RGB color combination found in multispectral remote sensing datasets [40–42]. The OIF is determined using Equation (1) [41]:

$$\text{OIF} = \frac{\text{Std}_i + \text{Std}_j + \text{Std}_k}{| \text{Corr}_{i,j} | + | \text{Corr}_{i,k} | + | \text{Corr}_{j,k} |} \quad (1)$$

Std_i is the standard deviation of band i , whereas $\text{Corr}_{i,j}$ shows the two bands' absolute correlation coefficients, i and j . Choosing the three bands with the greatest OIFs guarantees that the combination contains the most information while simultaneously demonstrating little correlation. This option is believed to provide the most detailed information and is used for improved lithological differentiation.

3.1.4. False-Color Composite (FCC)

The differentiation between the lithological and hydrothermal alteration zones was enhanced using strategies such as those recommended by Campbell, J. B., and Wynne, R. H. (2011) [43]. The use of false-color composites (FCCs) assists considerably in viewing images, leading to enhanced interpretation. In this study, we selected RGB combinations based on the exposed rock unit types, the results of previous studies, the outcomes of optimal index factor (OIF) investigations, and the spectral features of the datasets utilized, ensuring the maximum degree of discrimination.

3.1.5. Decorrelation Stretch (DS)

The use of DS can reveal nearly imperceptible images that are hardly visible to the naked eye. The heightened visibility of distinct variations in color can provide valuable indications of superposition. Images can be improved for publishing or presentation to viewers who may not have the ability or desire to decipher their subtle aspects. Decorrelation stretching is gaining popularity as a key method, as evidenced by [44–46] discussions in the literature. The obtained data are transformed using the principal component method. In this case, the modified channels can be contrast-stretched and arbitrarily allocated primary colors for display as a color composite image.

3.1.6. Band Rationing (BR)

The technique of dividing one band's digital number (DN) levels by the corresponding value of the DN of another band is known as band rationing. Following this step, a grayscale image with the DN values obtained is displayed, revealing the bands' respective intensities [47–49]. The BR technique helps distinguish lithological features and identify hydrothermal alterations [13,42].

3.1.7. Minimum Noise Fraction (MNF)

The MNF approach is employed in image processing to help distinguish random noise throughout datasets and enhance spectrum variance [50,51]. This approach was discovered to be effective in accurately identifying and categorizing various types of rocks, particularly when utilizing ASTER SWIR data. The (VNIR) and (SWIR) bands of (ASTER) were used to construct the MNF imagery for the research area.

3.1.8. Principal Component Analysis (PCA)

The PCA approach is widely recognized for its ability to decrease dimensionality, with the first principal component reflecting the most significant possible data variability.

Consequently, the primary principle components exhibit significant variation and are primarily employed to produce robust color composites, thereby enhancing the visual depiction of the mapping of the surface material [52–54]. In this work, we applied PCA to improve the lithological discrimination.

3.1.9. Independent Component Analysis (ICA)

The ICA method illustrates blind source separation (BSS), which separates the combined signals from the source signals without understanding the mixing method or the source signals [55]. As a result, the main objective of ICA is to find a set of uncorrelated components that are as independent of one another as is practical (note that uncorrelatedness is a less strict parameter than independence) [56]. As with PCA, we used the ICA approach to improve the lithological mapping.

4. Results and Discussion

4.1. Remote Sensing

4.1.1. Optimum Index Factor (OIF), False-Color Composite (FCC), and Decorrelation Stretch (DS)

The color composite image technique is commonly employed for displaying multi-spectral data. A band combination environment may show a picture utilizing only three primary colors: red, green, and blue. Reducing the variance value's correlation is crucial to obtaining the optimal choice among the three band combinations. The bands with higher OIF values (2, 3, and 5) for ASTER were chosen to enhance the extraction of different lithological information from the image (Figure 3a), as shown in Table 1. This table displays the highest OIF values and rankings of the combinations of ASTER bands. The ultramafic rocks are shown in deep red.

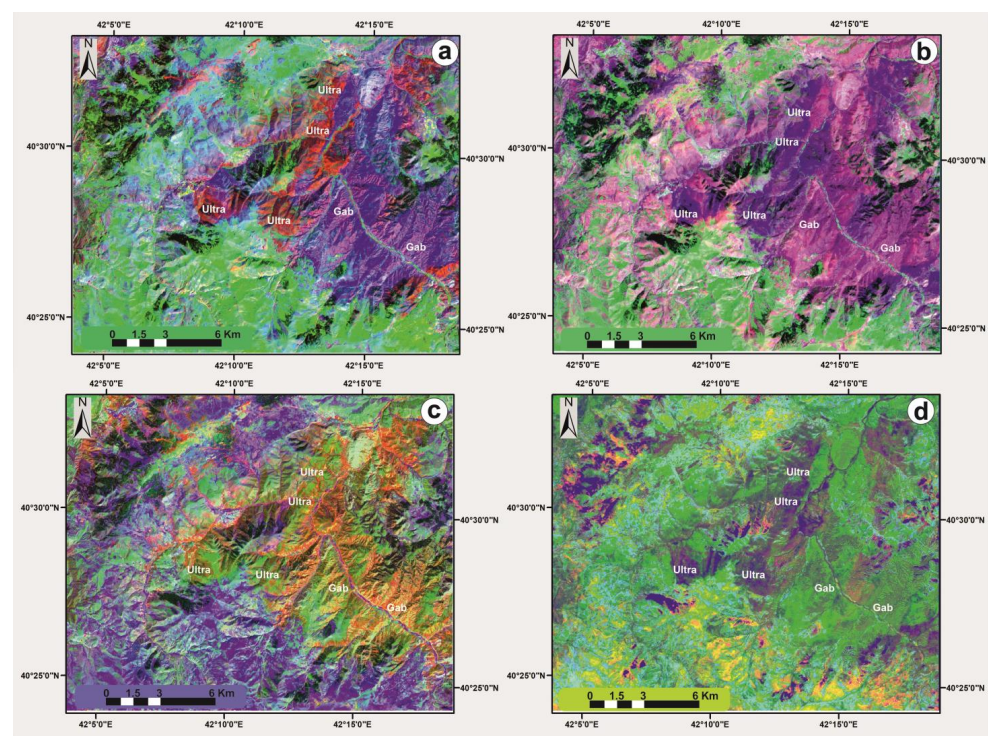


Figure 3. (a) False-color composite image in the RGB of ASTER bands (2, 3, 5). Ultra = ultramafic and Gab = gabbro; (b) false-color composite image in the RGB of ASTER bands (8, 3, 1); (c) false-color composite image in the RGB of ASTER bands (1, 2, 3); and (d) false-color composite image in the RGB of the ASTER band ratio ($4/8$, $4/1$, and $3/2 \times 4/3$).

Table 1. The highest values of OIF and ranks of combinations of ASTER bands are as follows.

1	B2	B3	B5	(284.41)
2	B2	B3	B9	(276.16)
3	B2	B3	B6	(268.20)
4	B2	B3	B7	(262.72)
5	B2	B3	B8	(259.15)
6	B1	B3	B5	(247.70)

Ultramafic rocks appeared in blue based on a false-color composite image (Figure 3b) comprising bands (8, 3, 1) in red, green, and blue. DS techniques were utilized to analyze the 1-2-3 ASTER VNIR bands. Based on the features of Figure 3c, the ophiolitic rocks have undergone clear differentiation from the country rocks. The exposed ultramafic rocks display hues ranging from greenish to reddish [57].

4.1.2. Band Rationing (BR) Results

The RGB of ASTER band ratios (4/8, 4/1, and $3/2 \times 4/3$) proposed by Rajendran, S., and Nasir, S., in 2019 discriminates the ultramafic rocks in the dark brown color (Figure 3d). Taking the absorption features of ferromagnesian minerals into account, [58] illustrated that the b3/b4 band ratio helps distinguish ultramafic rocks, such as dunites and serpentinite ultramafic units, which appear darker compared to other rocks (Figure 4a).

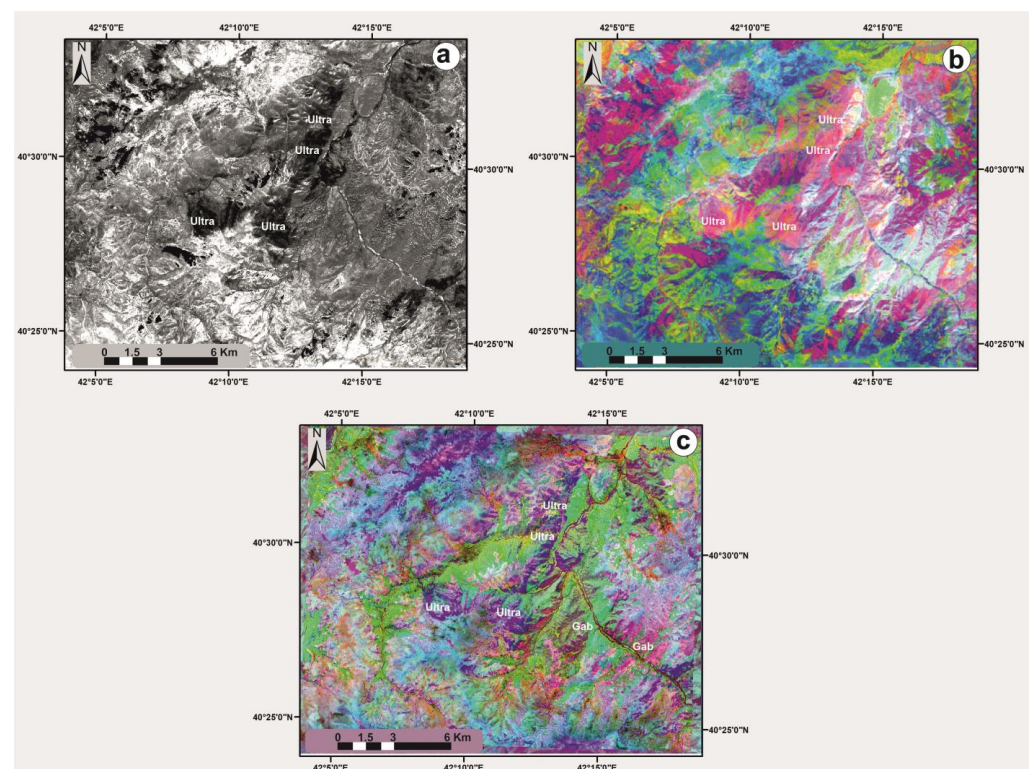


Figure 4. (a) Grayscale image of the ASTER band ratio (3/4), (b) false-color composite image in the RGB of ASTER MNF (1, 2, 3), and (c) false-color composite image in the RGB of ASTER MNF (9, 6, 4).

4.1.3. Minimum Noise Fraction (MNF) Results

The findings of our study indicate that the initial MNF bands, specifically MNF1, MNF2, and MNF3 in the RGB spectrum, exhibit superior lithological distinction due to their high information content and minimal noise compared to the following bands. For example, the MNF1, MNF2, and MNF3 RGB images displayed a remarkable distinction

between various rock types at the research location, especially the ultramafic rocks that appeared light pink in color (Figure 4b). The authors of [58] employed the MNF9, MNF6, and MNF4 components of the RGB ASTER data to efficiently distinguish ultramafic rocks, represented by the violet hue (Figure 4c).

4.1.4. Principal and Independent Component Analyses (PCA-ICA)

As approaches to dimensionality reduction and image improvement, PCA and ICA transformation generate bands with considerable information. These bands help determine the spectral properties of different rocks or minerals in the study area. To distinguish the bluish ultramafic rocks, three PCs (PC1, PC2, and PC3) in the false-color composite RGB image were created (Figure 5a). Conversely, the IC (ICA1, ICA2, and ICA3) false-color composite images in RGB successfully discriminate the ultramafic rocks in a light green color (Figure 5b).

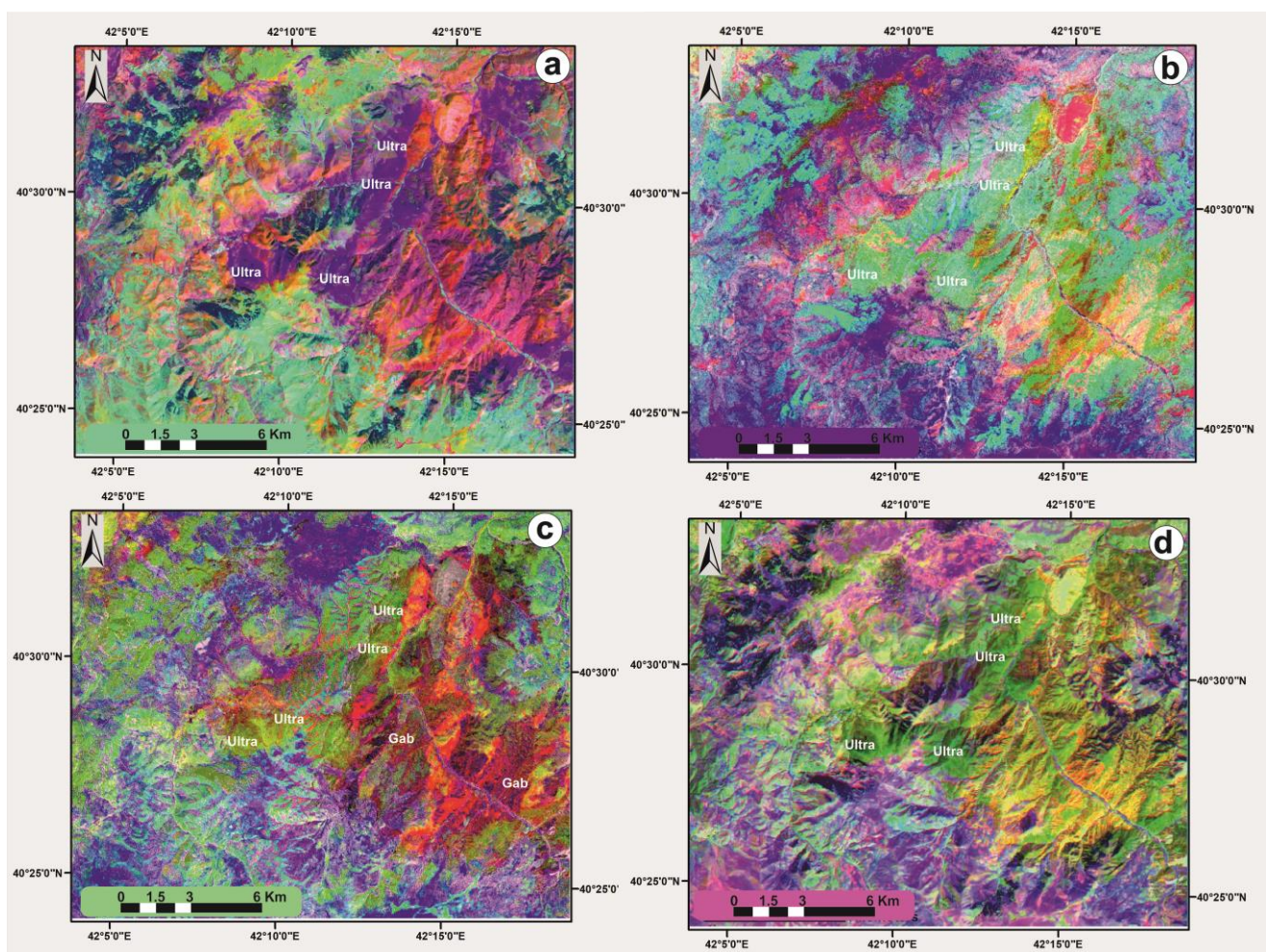


Figure 5. (a) False-color composite image in the RGB of ASTER PCs (1, 2, 3), (b) false-color composite image in the RGB of ASTER ICs (1, 2, 3), (c) false-color composite image in the RGB of ASTER PCs (5, 4, 2), and (d) false-color composite image in the RGB of ASTER (b4, PC1, PC2).

The authors of [15] suggest using PC5, PC4, and PC2 to more effectively differentiate serpentinized harzburgites from other ophiolitic rocks such as gabbros and metabasalt. These components were also proposed to identify the possible chromite mineralized zone. A comparison of the RGB composite images of PC5, PC4, and PC2 with the results of [15] is provided in Figure 5c. The greenish-yellow color inside the ultramafic rocks better defines the possible mineralized zone for chromitites [37].

Instead of using a false-color composite (FCC) image that integrated the original bands of the datasets, PC images were mixed with the original band image because PC images have a more significant image variance than typical FCC images. Consequently, the hybrid color composite image in [58] combined b4, PC1, and PC2 (Figure 5d). This hybrid combination identifies the ultramafic rocks in a clear green color.

4.2. Field Observations, Petrography, and Mineral and Whole-Rock Geochemical Results

To draw insights from interpretations of the remote sensing data, we re-evaluated the meticulously collected samples of ultramafic rocks (especially harzburgites) from multiple locations across the study area in terms of their mineral and whole-rock geochemical properties. Employing a trinocular polarizing and reflecting microscope, we also conducted detailed petrographic examinations of new thin sections encompassing peridotite (harzburgite and dunite) and pyroxenite and chromitite, but only for this current study. However, no new analytical procedures were performed, nor was any reanalysis conducted. Instead, we relied entirely on the pre-existing data published and analyzed by the author of [34]. These previously gathered data were carefully reviewed, evaluated, and interpreted to inform the findings and conclusions of the present investigation. The mineral and whole-rock geochemical analysis methods are described in [34].

The existence of harzburgites holds significant importance in exploring potential podiform chromite deposits (i.e., chromitites). From this perspective, the predominant lithology in the study area consists mainly of harzburgites, frequently interspersed with smaller amounts of dunite, wehrlite, pyroxenite, and occasional chromitite blocks (as depicted in Figure 6a–h). Therefore, for this investigation, our focus was primarily on the harzburgites spread over a wider area. This main segment of the ultramafic section within the Kırdağ ophiolite is characterized as medium-to-coarse-grained crystallized and partly serpentinized harzburgites. They typically exhibit a characteristic porphyroclastic texture, comprising over 85% volume of olivine and orthopyroxene, less than 3% volume of clinopyroxene (cpx), and approximately 1%–2% volume of chromian spinels and 10% volume of serpentine minerals. The orthopyroxene contents in the harzburgite samples are notably elevated, with the most prominent ones displaying coarse-grained textures and extensive deformation aligned parallel to the foliation and featuring a bent structure alongside clinopyroxene exsolution lamellae (Figure 7a,b).

Examinations of the dunite samples via petrographic analysis revealed predominantly equigranular textures, primarily consisting of olivine, chromian spinel, and smaller amounts of serpentine (Figure 7c,d). It was also determined that the pyroxenites are orthopyroxenites, have a coarse-grained texture, and consist entirely of orthopyroxene, except for a 1%–5% volume of clinopyroxene and spinel (Figure 7e). The chromitite samples underwent examination using a reflection microscope, revealing massive and semi-massive textures. Serpentinized olivines were seen in these samples alongside the chromian spinels (Figure 7f).

To achieve the aim of this study, our investigation of the mineral chemistry focused on pristine primary silicates and oxides, such as olivine, orthopyroxene, clinopyroxene, and chromian spinel, extracted from the harzburgites within the Kırdağ ophiolite. These harzburgitic peridotites serve as the foundational host rock for the dunites, chromitites, and pyroxenites.

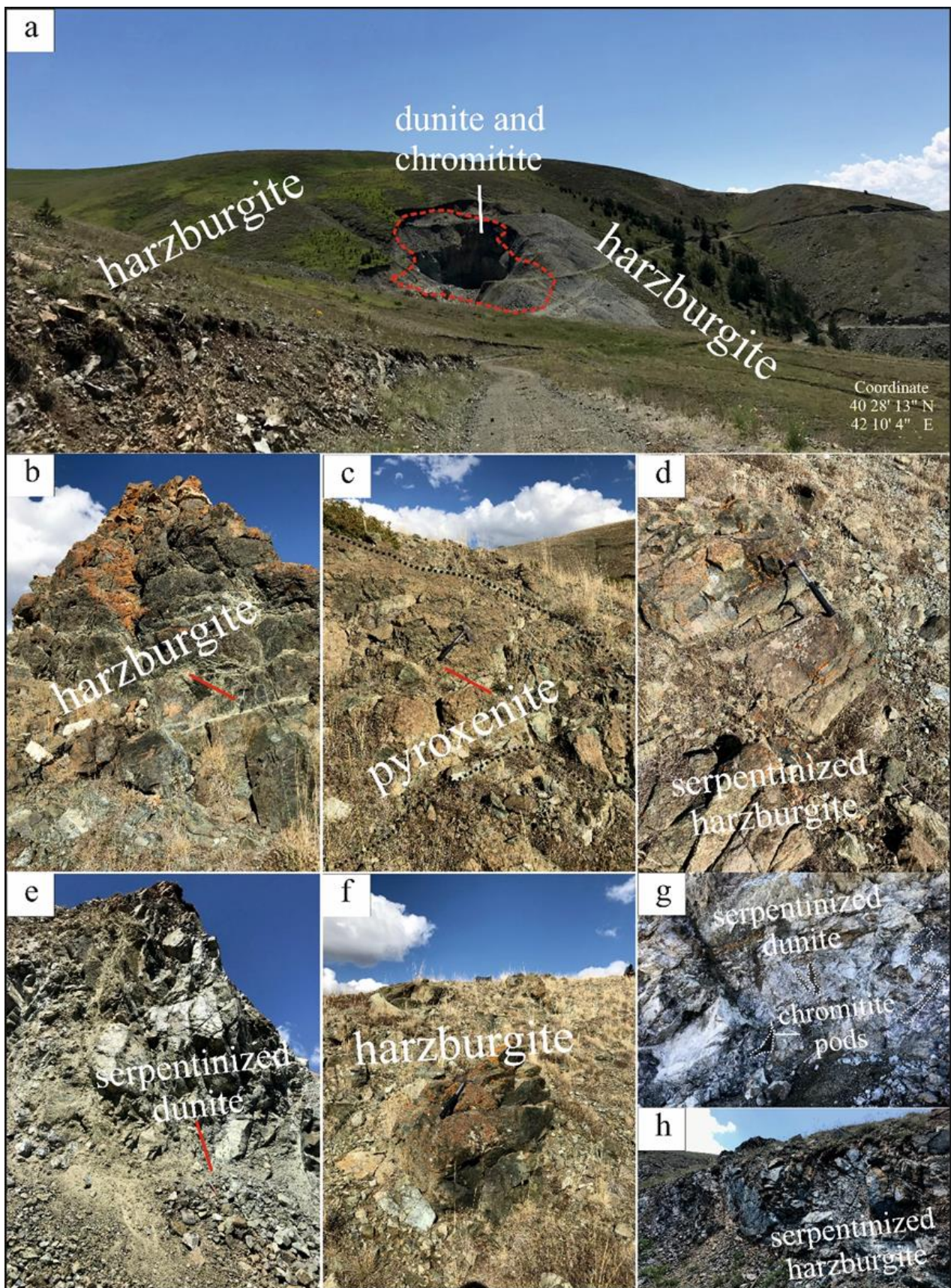


Figure 6. (a) Field snapshot exhibiting the juxtaposition between the host harzburgite and adjacent lithologies (including dunite, pyroxenite, and chromitite) within the research locale. (b–h) Detailed close-up images showcasing the characteristics of the harzburgite, dunite, pyroxenite, and chromitite pod within the mantle section of the Kırdağ ophiolite.

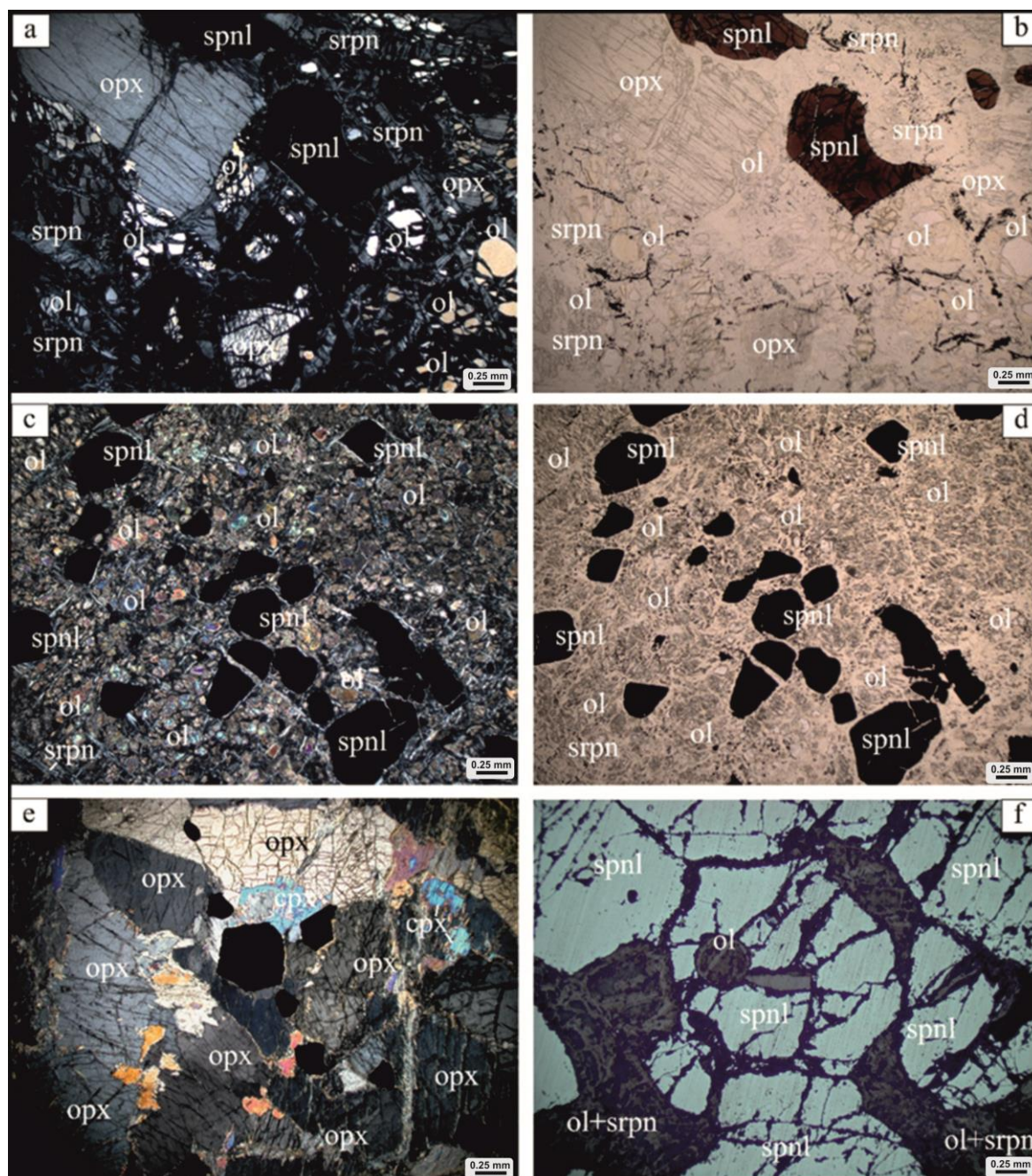


Figure 7. Thin-section photomicrographs of the harzburgite (a,b), dunite (c,d), pyroxenite (e), and chromitite (f). Microphotos (a,c,e) were taken under cross-polarized light, (b,d) were taken under plane-polarized light, and (f) was taken using a reflecting microscope for a chromitite ore sample. In the figure, spnl = chromian spinel, ol = olivine, opx = orthopyroxene, cpx = clinopyroxene, and srpn = serpentine.

The olivines in the harzburgites exhibit Fo-numbers ranging from 90.74 to 91.21, and their NiO and MnO contents vary between 0.39 and 0.50 and 0.09 and 0.15, respectively [34]. The FeO and Cr₂O₃ contents of the olivines also vary between 8.51 and 9.08 and 0.17 and 0.60, respectively [34]. Based on the microprobe analysis findings, the orthopyroxenes, which constitute the predominant minerals in harzburgites after olivines, exhibit an enstatite composition [34]. The major chemical compositions of the orthopyroxenes generally display slight variations within narrow ranges. The Mg-numbers (Mg/(Mg+Fe)) of the orthopyroxenes observed in harzburgite range from 0.91 to 0.94. Additionally, these orthopyroxenes' Al₂O₃ and TiO₂ contents are relatively uniform, falling within the ranges

of 1.07 to 1.83 wt.% and <0.01 to 0.03 wt.%, respectively [34]. Despite being relatively less abundant in these harzburgites, clinopyroxenes play a significant role in petrological interpretation, showcasing Mg-numbers ($Mg/(Mg+Fe)$) spanning from 0.94 to 0.95 [34]. The Al_2O_3 and TiO_2 concentrations within these clinopyroxenes vary, ranging from 1.47 to 2.13 wt.% and <0.01 to 0.01 wt.%, respectively [34]. Across all observed clinopyroxenes, the Cr_2O_3 content falls within the range of 0.61 to 1.30 (wt.%) [34]. The composition of chromian spinels within these harzburgites exhibited a high degree of uniformity. Specifically, the Cr-numbers ($Cr/(Cr+Al)$) of the chromian spinels fall within the range of 0.54 to 0.61 [34]. These spinels also demonstrate narrow ranges of Mg-numbers ($Mg/(Mg+Fe)$), spanning from 0.52 to 0.56. Moreover, their TiO_2 contents are notably low, measuring at 0.01 (wt.%) [34].

The whole-rock geochemical analyses conducted on the harzburgites within the Kırdağ ophiolite were re-evaluated for this current investigation. Substantial alterations were noted in the loss on ignition (LOI) values across all analyzed samples, reflecting varying degrees of alteration. These values exhibit a broad spectrum, ranging from 4 to 14.90 (wt.%). Their MgO contents range between 35.39 and 40.90 (wt.%); in comparison, the Al_2O_3 contents fall within the 0.40 to 0.64 wt.% range. In addition, the SiO_2 , Fe_2O_3 , CaO, MnO, and Cr_2O_3 contents (wt.%) vary from 39.66 to 45.49, 7.32 to 8.46, 0.33 to 0.80, 0.10 to 0.11, and 0.27 to 0.45, respectively. Conversely, the trace element compositions of the harzburgite show deficient concentrations [34].

4.3. Petrogenesis and Tectonic Implications in the Mantle Section of the Kırdağ Ophiolite

The mineral and whole-rock geochemical characteristics observed in harzburgite from the Kırdağ ophiolite (Erzurum, NE Turkey) offer compelling evidence for melting and melt-rock interactions during harzburgite generation [34]. The Cr-number, Mg-number, Fe^{3+} -number, and TiO_2 contents of chromian spinels are vital parameters utilized to discern the tectonic origins of peridotites [59–64]. The mentioned compositions of the chromian spinels in the harzburgites from the Kırdağ ophiolite imply their genesis within a supra-subduction zone setting (SSZ) ([34]; Figure 8a–c). The Mg-numbers and Al_2O_3 contents of orthopyroxene and clinopyroxene in mantle peridotites indicate partial melting and SSZ-related tectonic conditions [65–67]. The high Mg-number and low Al_2O_3 contents in the orthopyroxenes and clinopyroxenes of the Kırdağ ophiolite harzburgites are similar to those of fore-arc peridotites ([34]; Figure 8d,e). Additionally, whole-rock geochemical analysis of the harzburgite samples aligns with the mineral chemistry data, showing similarities to depleted fore-arc peridotites in terms of Al_2O_3/SiO_2 ratios and V (ppm) contents ([34]; Figure 8f).

In summary, the harzburgites within the Kırdağ ophiolite are not simply residual peridotites; they reflect a reactive origin influenced by both melt–peridotite interactions and the partial melting process in a fore-arc setting [34]. These characteristics also provide insights into the processes that may have led to the formation of chromitite orebodies in the Kırdağ ophiolite mantle section.

4.4. Integration of Remote Sensing and Geochemical Results

In mineral potential mapping, it is necessary to integrate several data sources in a spatial evaluation approach. A combined technique was utilized to determine the likely high-potential sites of chromitite. The results obtained from the remote sensing data and geochemical analysis were combined and produced significant proof, which can aid in the research techniques used in the exploration of chromitite.

Using various techniques, including OIF, FCC, BR, MNF, ICA, PCA, and DS, it was possible to use the remote sensing results to distinguish between peridotites (harzburgites) hosting chromitite and other lithologies (Figure 9). The existence of harzburgites significantly impacts chromite ore deposit prediction and identification.

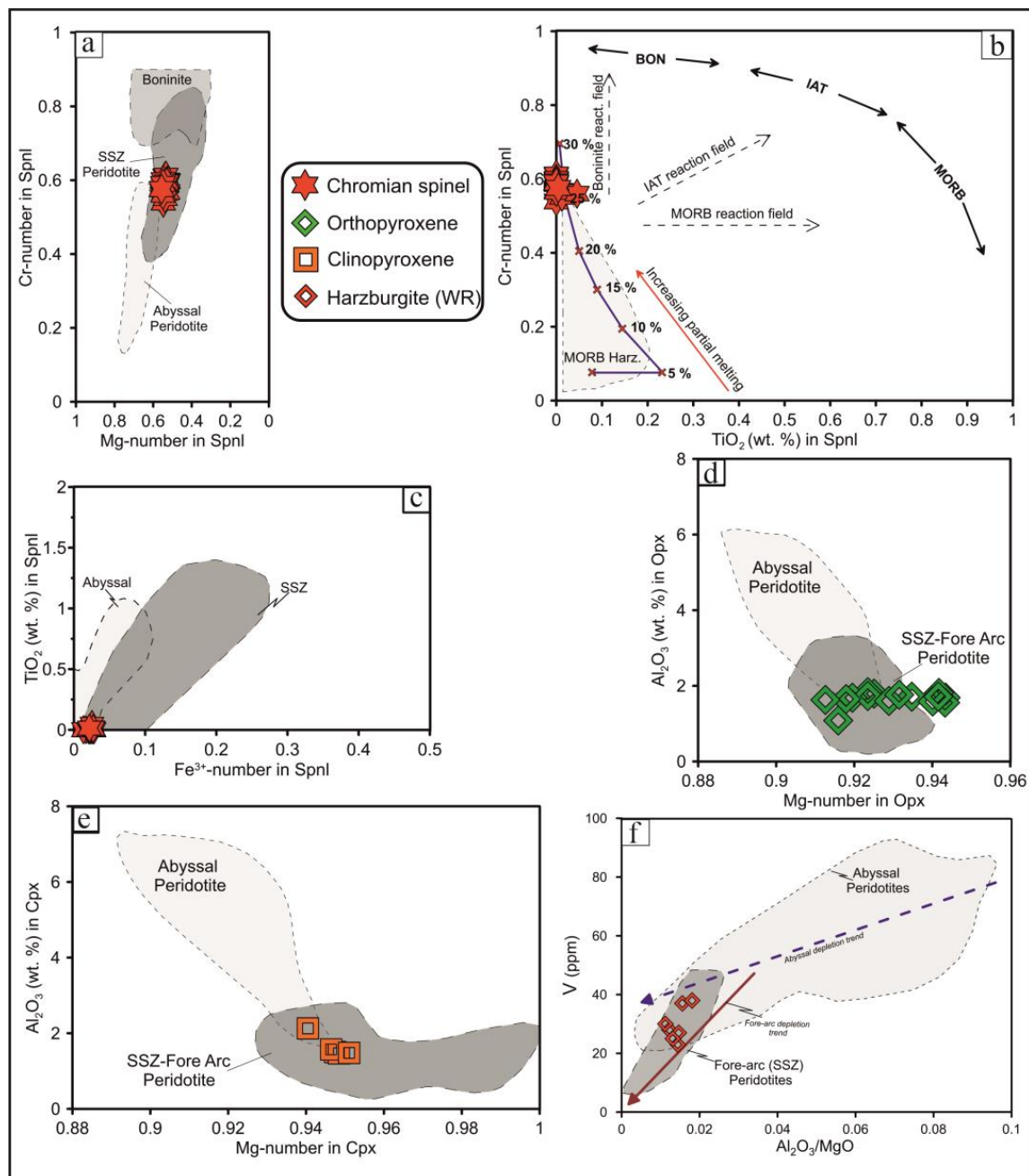


Figure 8. Graphical representations (a,b) illustrating the relationship between the Cr-number, Mg-number, and Cr-number and TiO_2 for chromian spinels within the harzburgite. Abyssal, fore-arc peridotite, and boninite fields are derived from [68], whereas the reaction fields and partial melting trend are referenced from [66,69], respectively. The diagram (c) presents the relationship between TiO_2 and Fe^{3+} -number for chromian spinels. The fields representing the Mid-Ocean Ridge (MOR) and Supra-Subduction Zone (SSZ) contexts are based on data from [64]. Diagram (d) illustrates the correlation between Al_2O_3 and Mg-number for orthopyroxene. In addition, (e) depicts the exact correlation for clinopyroxene. The fields representing abyssal and SSZ peridotites are based on data from [67]. The diagram (f) illustrates the relationship between V (ppm) and $\text{Al}_2\text{O}_3/\text{MgO}$ for the harzburgites from the Kırdağ ophiolite. The fields representing the fore-arc and abyssal peridotites are derived from data compiled by [65,67], respectively.

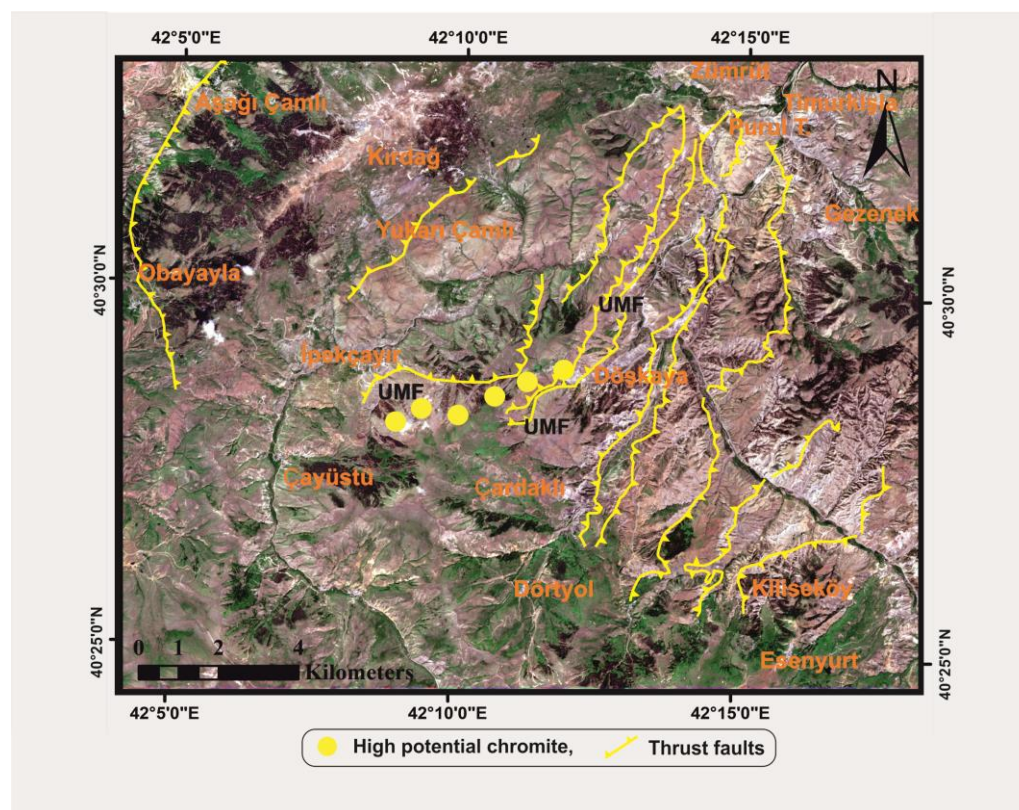


Figure 9. Sentinel-2-L2A True Color B4, B3, B2 showing the location of high-potential chromite-bearing mineralized zones based on integrating remote sensing and geochemical results with field validation.

The study results suggest that the east of the Oltu site has numerous areas with high chromite potential. The triangle areas between İpekçayır, Çayüstü, and Döşkaya are prospective high-potential chromite-bearing mineralized zones within the ophiolite region and successfully mapped serpentized harzburgite-containing chromite orebodies (Figure 9). It is strongly recommended that this technique be employed rather than depending entirely on field data to explore chromitite in arid locations worldwide further.

5. Conclusions

The region of East Oltu Erzurum, Turkey, which comprises the Kırdağ ophiolite sequence, including the study area, and is situated in the Erzurum–Kars Ophiolite Zone, serves as the case study. The primary goal of the present research was to apply comprehensive exploration techniques that integrate mineral and whole-rock geochemical data with remote sensing data to find and identify locations of high-potential sites of chromite mineralization in a complex geological location, particularly in mountainous terranes with rough topographies. Additionally, through this research, we aimed to differentiate highly serpentized peridotites harboring chromite mineralization from other ultramafic and mafic rocks. The following techniques were used to identify hydrothermal alteration zones and distinguish lithological features: PCA-ICA, BR, MNF, DS, OIF, and FCC. Previously published mineral and whole-rock geochemical data of the harzburgites, the most common lithology in the study area, were used to validate the remote sensing data in this study. In addition, using a trinocular polarizing and reflecting microscope, we conducted comprehensive petrographic examinations of new thin sections of peridotites (harzburgite and dunite), pyroxenite, and chromitite specifically for this study.

The remote sensing results showed that the ultramafic rocks that host chromitite orebodies were successfully detected, and their spectral variation was identified. The presence of harzburgites significantly influences the identification of predicted chromite ore deposits. The harzburgite's mineral geochemical characteristics demonstrate petrological processes and

associated tectonic environments. The chromian spinels' Cr, Mg, Fe³⁺, and TiO₂ compositions in the harzburgites indicate the subduction zone in which they formed. Moreover, the partial melting conditions in mantle peridotites are marked by the Mg-numbers, TiO₂, and Al₂O₃ levels of orthopyroxene and clinopyroxene. By investigating the harzburgites of the Kırdağ ophiolite, it is evident from these parameters that they have experienced significant partial melting and melt interactions in a subduction zone environment.

Furthermore, the results of the whole-rock geochemical analysis of the harzburgite samples are in good agreement with the results of the mineral chemistry investigation; in particular, they show that the Al₂O₃/SiO₂ ratios and V (ppm) concentrations of the samples are similar to those of depleted fore-arc peridotites. In particular, it is crucial to comprehend that the harzburgites discovered inside the Kırdağ ophiolite are reactive since the processes of melt interaction in peridotites play an essential role in the formation of chromitite zones. The study results suggest that the east of the Oltu area comprises numerous areas with high chromitite-bearing zones within the ophiolite region, and we mapped the serpentinized harzburgite-containing dunite and chromitite in the triangle area between İpekçayır, Çayüstü, and Döşkaya sites. The combined strategies provide significant benefits over traditional exploration methods, reinforcing the site's potential for future chromitite production.

Author Contributions: Conceptualization, A.A.E.-R., F.D., Ö.B. and S.T.; data curation, Ö.B., I.A. and S.T.; formal analysis, F.D., Ö.B. and I.A.; funding acquisition, K.A. and M.S.F.; investigation, Ö.B. and I.A.; methodology, A.A.E.-R., F.D., Ö.B. and S.T.; project administration, K.A. and M.S.F.; resources, A.A.E.-R. and O.A.; software, A.A.E.-R., F.D., Ö.B., I.A. and S.T.; supervision, A.A.E.-R., F.D. and Ö.B.; validation, F.D., Ö.B., I.A. and S.T.; visualization, A.A.E.-R., F.D., Ö.B. and I.A.; writing—original draft, A.A.E.-R., F.D., Ö.B. and I.A.; writing—review and editing, A.A.E.-R., I.A., L.J. and O.A. All authors have read and agreed to the published version of the manuscript.

Funding: This research was supported by Researchers Supporting Project number (RSP2024R249), King Saud University, Riyadh, Saudi Arabia, and Sichuan Science and Technology Program (2023NS-FSC0777).

Data Availability Statement: Data can be made available by the corresponding authors upon reasonable request.

Acknowledgments: The authors thank the editors and reviewers for their valuable comments and suggestions.

Conflicts of Interest: The authors declare no conflicts of interest.

References

1. Papp, J.F.; Lipin, B.R. *Chromite Industrial Minerals & Rocks: Commodities, Markets, and Uses*, 7th ed.; SME: Southfield, MI, USA, 2006.
2. Abu El Ela, F.F.; Farahat, E.S. Neoproterozoic podiform chromitites in serpentinites of the Abu Meriewa–Hagar Dungash district, Eastern Desert, Egypt: Geotectonic implications and metamorphism. *Isl. Arc* **2010**, *19*, 151–164. [CrossRef]
3. González-Jiménez, J.M.; Proenza, J.A.; Gervilla, F.; Melgarejo, J.C.; Blanco-Moreno, J.A.; Ruiz-Sánchez, R.; Griffin, W.L. High-Cr and high-Al chromitites from the Sagua de Tánamo district, Mayarí-Cristal ophiolitic massif (eastern Cuba): Constraints on their origin from mineralogy and geochemistry of chromian spinel and platinum-group elements. *Lithos* **2011**, *125*, 101–121. [CrossRef]
4. Grieco, G.; Merlini, A. Chromite alteration processes within Vourinos ophiolite. *Int. J. Earth Sci.* **2012**, *101*, 1523–1533. [CrossRef]
5. Ahmed, A.H. Highly depleted harzburgite–dunite–chromitite complexes from the Neoproterozoic ophiolite, south Eastern Desert, Egypt: A possible recycled upper mantle lithosphere. *Precambrian Res.* **2013**, *233*, 173–192. [CrossRef]
6. Moghadam, H.S.; Stern, R.J. Ophiolites of Iran: Keys to understanding the tectonic evolution of SW Asia:(I) Paleozoic ophiolites. *J. Asian Earth Sci.* **2014**, *91*, 19–38. [CrossRef]
7. Dilek, Y. Ophiolite pulses, mantle plumes and orogeny. *Geol. Soc. Lond. Spec. Publ.* **2003**, *218*, 9–19. [CrossRef]
8. Pearce, J.A. Supra-Subduction Zone Ophiolites: The Search for Modern Analogues. 2003. Available online: <http://repository.geologyscience.ru/handle/123456789/35668> (accessed on 27 May 2024).
9. Abd El-Raouf, A.; Doğru, F.; Abdelrahman, K.; Fnais, M.S.; El Manharawy, A.; Amer, O. Using Airborne Geophysical and Geochemical Methods to Map Structures and Their Related Gold Mineralization. *Minerals* **2023**, *13*, 237. [CrossRef]
10. Mosier, D.L.; Singer, D.A.; Moring, B.C.; Galloway, J.P. *Podiform Chromite Deposits—Database and Grade and Tonnage Models*; U.S. Geological Survey: Reston, VA, USA, 2012.

11. Hornicka, E.; Targosz, P.; Loska, M.; Wojdyła, M. Complex Geophysical Investigation in Search of Chromite Deposits at Ljuboten Greenfield Site. In Proceedings of the NSG2020 3rd Conference on Geophysics for Mineral Exploration and Mining, Online, 7–8 December 2020; European Association of Geoscientists & Engineers: Utrecht, The Netherlands, 2020; pp. 1–5.
12. Kharbish, S.; Eldosouky, A.M.; Amer, O. Integrating mineralogy, geochemistry and aeromagnetic data for detecting Fe–Ti ore deposits bearing layered mafic intrusion, Akab El-Negum, Eastern Desert, Egypt. *Sci. Rep.* **2022**, *12*, 15474. [\[CrossRef\]](#)
13. El-Raouf, A.A.; Doğru, F.; Azab, I.; Jiang, L.; Abdelrahman, K.; Fnais, M.S.; Amer, O. Utilizing Remote Sensing and Satellite-Based Bouguer Gravity data to Predict Potential Sites of Hydrothermal Minerals and Gold Deposits in Central Saudi Arabia. *Minerals* **2023**, *13*, 1092. [\[CrossRef\]](#)
14. Gad, S.; Kusky, T. Lithological mapping in the Eastern Desert of Egypt, the Barramiya area, using Landsat thematic mapper (TM). *J. Afr. Earth Sci.* **2006**, *44*, 196–202. [\[CrossRef\]](#)
15. Amer, R.; Kusky, T.; Ghulam, A. Lithological mapping in the Central Eastern Desert of Egypt using ASTER data. *J. Afr. Earth Sci.* **2010**, *56*, 75–82. [\[CrossRef\]](#)
16. Pournamdari, M.; Hashim, M.; Pour, A.B. Application of ASTER and Landsat TM Data for Geological Mapping of Esfandagheh Ophiolite Complex, Southern Iran. *Resour. Geol.* **2014**, *64*, 233–246. [\[CrossRef\]](#)
17. Sabins, F.F. Remote sensing for mineral exploration. *Ore Geol. Rev.* **1999**, *14*, 157–183. [\[CrossRef\]](#)
18. Van Der Meer, F.D.; Van Der Werff, H.M.A.; Van Ruitenbeek, F.J.A.; Hecker, C.A.; Bakker, W.H.; Noomen, M.F.; Van Der Meijde, M.; Carranza, E.J.M.; Smeth, J.B.D.; Woldai, T. Multi- and hyperspectral geologic remote sensing: A review. *Int. J. Appl. Earth Obs. Geoinf.* **2012**, *14*, 112–128. [\[CrossRef\]](#)
19. Rajendran, S.; Al-Khirbash, S.; Pracejus, B.; Nasir, S.; Al-Abri, A.H.; Kusky, T.M.; Ghulam, A. ASTER detection of chromite bearing mineralized zones in Semail Ophiolite Massifs of the northern Oman Mountains: Exploration strategy. *Ore Geol. Rev.* **2012**, *44*, 121–135. [\[CrossRef\]](#)
20. Rajendran, S.; Nasir, S. Mapping of hydrothermal alteration in the upper mantle-lower crust transition zone of the Tayin Massif, Sultanate of Oman using remote sensing technique. *J. Afr. Earth Sci.* **2019**, *150*, 722–743. [\[CrossRef\]](#)
21. MAT. 1:500,000 Scale Geology Map of Turkey; The General Directorate of Mineral Research and Exploration (MTA): Ankara, Turkey, 2002.
22. Okay, A.I.; Tüysüz, O. Tethyan sutures of northern Turkey. *Geol. Soc. Lond. Spec. Publ.* **1999**, *156*, 475–515. [\[CrossRef\]](#)
23. Konak, N.; Hakyemez, H.; Bilgiç, T.; Bilgin, R.; Hepşen, N.; Ercan, T. Oltu-Olur-Şenkaya-Narman-Uzundere-Yusufeli. In *Geology of Northeast Pontides*; The General Directorate of Mineral Research and Exploration (MTA): Ankara, Turkey, 2001; p. 10489.
24. Şengör, A.C.; Yilmaz, Y. Tethyan evolution of Turkey: A plate tectonic approach. *Tectonophysics* **1981**, *75*, 181–241. [\[CrossRef\]](#)
25. Okay, A.; Sahintürk, O. Geology of the Eastern Pontides. Available online: https://www.researchgate.net/profile/Aral-Okay-2/publication/279480387_AAPG_Memoir_68_Regional_and_Petroleum_Geology_of_the_Black_Sea_and_Surrounding_Region_Chapter_15_Geology_of_the_Eastern_Pontides/links/55be634608aed621de121107/AAPG-Memoir-68-Regional-and-Petroleum-Geology-of-the-Black-Sea-and-Surrounding-Region-Chapter-15-Geology-of-the-Eastern-Pontides.pdf (accessed on 17 July 2024).
26. Şengör, A.M.C.; Özeren, S.; Genç, T.; Zor, E. East Anatolian high plateau as a mantle-supported, north-south shortened domal structure. *Geophys. Res. Lett.* **2003**, *30*, 2003GL017858. [\[CrossRef\]](#)
27. Ustaömer, T.; Robertson, A.H.F. Late Palaeozoic–Early Cenozoic tectonic development of the Eastern Pontides (Artvin area), Turkey: Stages of closure of Tethys along the southern margin of Eurasia. *Geol. Soc. Lond. Spec. Publ.* **2010**, *340*, 281–327. [\[CrossRef\]](#)
28. Dewey, J.F.; Pitman, W.C., III; Ryan, W.B.; Bonnin, J. Plate tectonics and the evolution of the Alpine system. *Geol. Soc. Am. Bull.* **1973**, *84*, 3137–3180. [\[CrossRef\]](#)
29. Robertson, A.H.F.; Dixon, J.E. *Introduction: Aspects of the Geological Evolution of the Eastern Mediterranean*; The Geological Society of London: London, UK, 1984; Volume 17, pp. 1–74. ISBN 0305-8719.
30. Sarifakioğlu, E.; Özen, H.; Winchester, J.A. Petrogenesis of the Refahiye Ophiolite and its tectonic significance for Neotethyan ophiolites along the Izmir–Ankara–Erzincan Suture Zone. *Turk. J. Earth Sci.* **2009**, *18*, 187–207.
31. Parlak, O.; Çolakoğlu, A.; Dönmez, C.; Sayak, H.; Yildirim, N.; Türkel, A.; Odabaşı, İ. Geochemistry and tectonic significance of ophiolites along the İzmir–Ankara–Erzincan Suture Zone in northeastern Anatolia. *Geol. Soc. Lond. Spec. Publ.* **2013**, *372*, 75–105. [\[CrossRef\]](#)
32. Robertson, A.; Parlak, O.; Ustaömer, T.; Taşlı, K.; İnan, N.; Dumitrica, P.; Karaoğlu, F. Subduction, ophiolite genesis and collision history of Tethys adjacent to the Eurasian continental margin: New evidence from the Eastern Pontides, Turkey. *Geodin. Acta* **2013**, *26*, 230–293. [\[CrossRef\]](#)
33. Uysal, I.; Ersoy, E.Y.; Dilek, Y.; Escayola, M.; Sarifakioğlu, E.; Saka, S.; Hirata, T. Depletion and refertilization of the Tethyan oceanic upper mantle as revealed by the early Jurassic Refahiye ophiolite, NE Anatolia—Turkey. *Gondwana Res.* **2015**, *27*, 594–611. [\[CrossRef\]](#)
34. Bilici, Ö. Reactive harzburgite and ultimate dunite formation as a result of boninite-like melt interaction: Petrological evidence from the Kırdağ ophiolite (Erzurum, NE Turkey). *J. Afr. Earth Sci.* **2022**, *193*, 104601. [\[CrossRef\]](#)
35. Konak, N.; Sumengen, M. 1/100,000 Scale Turkish Geology Map Series, Kars-H48 Sheet; The General Directorate of Mineral Research and Exploration (MTA): Ankara, Turkey, 2009; Volume 106, p. 23.

36. Abrams, M. The Advanced Spaceborne Thermal Emission and Reflection Radiometer (ASTER): Data products for the high spatial resolution imager on NASA's Terra platform. *Int. J. Remote Sens.* **2000**, *21*, 847–859. [\[CrossRef\]](#)
37. Rajendran, S.; Nasir, S.; Kusky, T.M.; Ghulam, A.; Gabr, S.; El-Ghali, M.A.K. Detection of hydrothermal mineralized zones associated with listwaenites in Central Oman using ASTER data. *Ore Geol. Rev.* **2013**, *53*, 470–488. [\[CrossRef\]](#)
38. Yamaguchi, Y.; Kahle, A.B.; Tsu, H.; Kawakami, T.; Pniel, M. Overview of advanced spaceborne thermal emission and reflection radiometer (ASTER). *IEEE Trans. Geosci. Remote Sens.* **1998**, *36*, 1062–1071. [\[CrossRef\]](#)
39. Javhar, A.; Chen, X.; Jovid, A.; Yunus, M.; Jamshed, A.; Eldiir, D.; Zulfiyor, B. Evaluation of remote sensing techniques for lithological mapping in the southeastern Pamir using Landsat 8 OLI data. *Int. J. Geoinform.* **2018**, *14*, 1–10.
40. Chavez, P.S.; Berlin, G.L.; Sowers, L.B. Statistical method for selecting Landsat MSS ratios. *J. Appl. Photogr. Eng.* **1982**, *8*, 23–30.
41. Chavez, P.S., Jr. Image Processing techniques for Thematic Mapper data. *Proc. ASPRS-ACSM Tech. Pap.* **1984**, *2*, 728–742.
42. Abdelkader, M.A.; Watanabe, Y.; Shebl, A.; El-Dokouny, H.A.; Dawoud, M.; Csámer, Á. Effective delineation of rare metal-bearing granites from remote sensing data using machine learning methods: A case study from the Umm Naggat Area, Central Eastern Desert, Egypt. *Ore Geol. Rev.* **2022**, *150*, 105184. [\[CrossRef\]](#)
43. Campbell, J.B.; Wynne, R.H. *Introduction to Remote Sensing*; Guilford Press: New York, NY, USA, 2011.
44. Gillespie, R.; Kahle, A.B.; Walker, R.E. Color enhancement of highly correlated images. I. Decorrelation and HSI contrast stretches. *Remote Sens. Environ.* **1986**, *20*, 209–235. [\[CrossRef\]](#)
45. Rothery, D.A. Improved discrimination of rock units using Landsat Thematic Mapper imagery of the Oman ophiolite. *J. Geol. Soc.* **1987**, *144*, 587–597. [\[CrossRef\]](#)
46. Abrams, M.J.; Rothery, D.A.; Pontual, A. Mapping in the Oman ophiolite using enhanced Landsat Thematic Mapper images. *Tectonophysics* **1988**, *151*, 387–401. [\[CrossRef\]](#)
47. Goetz, A.F.; Rowan, L.C.; Kingston, M.J. Mineral identification from orbit: Initial results from the shuttle multispectral infrared radiometer. *Science* **1982**, *218*, 1020–1024. [\[CrossRef\]](#)
48. Mars, J.C.; Rowan, L.C. Regional mapping of phyllic-and argillic-altered rocks in the Zagros magmatic arc, Iran, using Advanced Spaceborne Thermal Emission and Reflection Radiometer (ASTER) data and logical operator algorithms. *Geosphere* **2006**, *2*, 161–186. [\[CrossRef\]](#)
49. Pour, A.B.; Hashim, M. Hydrothermal alteration mapping from Landsat-8 data, Sar Cheshmeh copper mining district, south-eastern Islamic Republic of Iran. *J. Taibah Univ. Sci.* **2015**, *9*, 155–166. [\[CrossRef\]](#)
50. Green, A.A.; Berman, M.; Switzer, P.; Craig, M.D. A transformation for ordering multispectral data in terms of image quality with implications for noise removal. *IEEE Trans. Geosci. Remote Sens.* **1988**, *26*, 65–74. [\[CrossRef\]](#)
51. Kalinowski, A.; Oliver, S. ASTER mineral index processing manual. *Remote Sens. Appl. Geosci. Aust.* **2004**, *37*, 36–37.
52. Pearson, K.L., III. On lines and planes of closest fit to systems of points in space. *Lond. Edinb. Dublin Philos. Mag. J. Sci.* **1901**, *2*, 559–572. [\[CrossRef\]](#)
53. Sabins, F.F., Jr.; Ellis, J.M. *Remote Sensing: Principles, Interpretation, and Applications*; Waveland Press: Lake Zurich, IL, USA, 2020.
54. Ousmanou, S.; Fozing, E.M.; Kwékam, M.; Fodoue, Y.; Jeatsa, L.D.A. Application of remote sensing techniques in lithological and mineral exploration: Discrimination of granitoids bearing iron and corundum deposits in southeastern Banyo, Adamawa region-Cameroon. *Earth Sci. Inform.* **2023**, *16*, 259–285. [\[CrossRef\]](#)
55. Cardoso, J.-F. Blind signal separation: Statistical principles. *Proc. IEEE* **1998**, *86*, 2009–2025. [\[CrossRef\]](#)
56. Castella, M. Unsupervised Linear Component Analysis for a Class of Probability Mixture Models. *IEEE Signal Process. Lett.* **2024**, *31*, 31–35. [\[CrossRef\]](#)
57. Ekici, T. Lithological mapping of ophiolitic rocks from southern part of the Sivas Basin (Turkey) using ASTER imagery. *Turk. J. Earth Sci.* **2023**, *32*, 200–213. [\[CrossRef\]](#)
58. Çörtük, R.M.; Çelik, Ö.F.; Alkan, A.; Özkan, M.; Özyavaş, A. Distribution of rocks in Pınarbaşı Ophiolite from central Anatolia (Turkey) based on analysis of ASTER and Landsat-8 data. *Geol. J.* **2020**, *55*, 6810–6822. [\[CrossRef\]](#)
59. Rollinson, H. The geochemistry of mantle chromitites from the northern part of the Oman ophiolite: Inferred parental melt compositions. *Contrib. Mineral. Petrol.* **2008**, *156*, 273–288. [\[CrossRef\]](#)
60. Pagé, P.; Barnes, S.-J. Using trace elements in chromites to constrain the origin of podiform chromitites in the Thetford Mines ophiolite, Québec, Canada. *Econ. Geol.* **2009**, *104*, 997–1018. [\[CrossRef\]](#)
61. Dick, H.J.; Bullen, T. Chromian spinel as a petrogenetic indicator in abyssal and alpine-type peridotites and spatially associated lavas. *Contrib. Mineral. Petrol.* **1984**, *86*, 54–76. [\[CrossRef\]](#)
62. Arai, S. Characterization of spinel peridotites by olivine-spinel compositional relationships: Review and interpretation. *Chem. Geol.* **1994**, *113*, 191–204. [\[CrossRef\]](#)
63. Hellebrand, E.; Snow, J.E.; Dick, H.J.; Hofmann, A.W. Coupled major and trace elements as indicators of the extent of melting in mid-ocean-ridge peridotites. *Nature* **2001**, *410*, 677–681. [\[CrossRef\]](#) [\[PubMed\]](#)
64. Arai, S.; Okamura, H.; Kadoshima, K.; Tanaka, C.; Suzuki, K.; Ishimaru, S. Chemical characteristics of chromian spinel in plutonic rocks: Implications for deep magma processes and discrimination of tectonic setting. *Isl. Arc.* **2011**, *20*, 125–137. [\[CrossRef\]](#)
65. Parkinson, I.J.; Pearce, J.A. Peridotites from the Izu–Bonin–Mariana forearc (ODP Leg 125): Evidence for mantle melting and melt–mantle interaction in a supra-subduction zone setting. *J. Petrol.* **1998**, *39*, 1577–1618. [\[CrossRef\]](#)
66. Pearce, J.A.; Barker, P.F.; Edwards, S.J.; Parkinson, I.J.; Leat, P.T. Geochemistry and tectonic significance of peridotites from the South Sandwich arc–basin system, South Atlantic. *Contrib. Mineral. Petrol.* **2000**, *139*, 36–53. [\[CrossRef\]](#)

67. Choi, S.H.; Shervais, J.W.; Mukasa, S.B. Supra-subduction and abyssal mantle peridotites of the Coast Range ophiolite, California. *Contrib. Mineral. Petrol.* **2008**, *156*, 551–576. [[CrossRef](#)]
68. Tamura, A.; Arai, S. Harzburgite–dunite–orthopyroxenite suite as a record of supra-subduction zone setting for the Oman ophiolite mantle. *Lithos* **2006**, *90*, 43–56. [[CrossRef](#)]
69. Ozawa, K. Melting and melt segregation in the mantle wedge above a subduction zone: Evidence from the chromite-bearing peridotites of the Miyamori ophiolite complex, northeastern Japan. *J. Petrol.* **1994**, *35*, 647–678. [[CrossRef](#)]

Disclaimer/Publisher’s Note: The statements, opinions and data contained in all publications are solely those of the individual author(s) and contributor(s) and not of MDPI and/or the editor(s). MDPI and/or the editor(s) disclaim responsibility for any injury to people or property resulting from any ideas, methods, instructions or products referred to in the content.